



Earthquake source parameters estimated from high-rate multi-GNSS data: a case study of the 2022 *M*6.9 Menyuan earthquake

Xuechuan Li¹ · Changyun Chen¹ · Hongbao Liang¹ · Yu Li^{2,3} · Wei Zhan¹

Received: 30 July 2022 / Accepted: 7 December 2022 / Published online: 23 December 2022

© The Author(s) under exclusive licence to Institute of Geophysics, Polish Academy of Sciences & Polish Academy of Sciences 2022

Abstract

The epicenter, origin time, and magnitude of the earthquake are critical earthquake source parameters, as they can provide data support for earthquake emergency rescue and earthquake risk research, among others. Here, the high-rate displacement time series of 11 Global Navigation Satellite System (GNSS) stations during the 2022 Menyuan *M*6.9 earthquake were acquired using GPS, GPS/GLONASS, and GPS/GLONASS/Galileo observations using the PRIDE PPP-AR software. Our analysis revealed that the root mean squares (RMS) of displacement derived from GPS/GLONASS/Galileo relative to GPS-derived in the north, east, and up components were improved by 23.3, 34.4, and 24.4%, respectively. The epicenter location of the Menyuan earthquake based on GPS/GLONASS/Galileo-derived time series of each station was 101.201°E and 37.791°N, the earthquake origin time was 17:45:23.7 (UTC), and the moment magnitude was 6.62, which were more accurate than the GPS and GPS/GLONASS results. Although there was no significant advantage of calculating the coseismic displacement by multi-day static solution from GPS/GLONASS/Galileo, our results showed that the multi-GNSS combination can improve the stability of time series and reduce noise, and more realistically describe the surface displacement changes during earthquakes; accuracy of earthquake source parameters estimation, can, therefore, be improved with the use of multi-GNSS data.

Keywords Multi-GNSS · Epicenter location · Earthquake origin time · Moment magnitude · Coseismic displacement

Introduction

After occurrence of an earthquake, accurately obtaining parameters such as earthquake origin time, epicenter location, and magnitude can provide crucial information for earthquake warning, hazard assessment, and rescuing victims. Traditionally, instruments such as strong motion seismographs and seismometers have been used to record seismic wave signals; however, when a large earthquake occurs, these instruments can experience range saturation and, consequently, underestimate the earthquake magnitude.

In addition, baseline deviation due to human- or earthquake-induced instrument drift can cause errors in the estimation of seismic parameters obtained with these instruments. Alternatively, using high-rate (1–50 Hz) Global Navigation Satellite System (GNSS) observations can efficiently and accurately obtain the instantaneous state of motion during and after a seismic event. This method has become increasingly popular among seismologists due to its unlimited range and lack of accumulated error (Yin et al. 2010; Shan et al. 2019; Li et al. 2021a). For instance, Yin et al. (2018) used high-rate GPS data from seven stations near the Wenchuan earthquake location (Sichuan, China) to determine its epicenter, which was found to be 15.5 km away from that obtained using seismometry. They also discussed the statistical relationship between high-rate coseismic displacement and earthquake intensity. Fang et al. (2020) constructed an empirical formula for the relationship between peak ground velocity (PGV) and seismic moment magnitude using high-rate GPS data from 22 earthquakes. The difference between the calculated magnitude and the actual magnitude was 0.26 magnitude units. Gao et al. (2021) used high-rate data from 55 continuous GPS stations surrounding the Maduo earthquake

Edited by Prof. Maria Marsella (ASSOCIATE EDITOR) / Prof. Ramón Zúñiga (CO-EDITOR-IN-CHIEF).

✉ Xuechuan Li
leexc0124@163.com

¹ The First Monitoring and Application Center, China Earthquake Administration, Tianjin, China

² Institute of Geophysics, China Earthquake Administration, Beijing 100081, China

³ China Earthquake Networks Center, Beijing 100045, China

(Qinghai Province, China) and inverted its moment magnitude based on peak ground displacement (PGD) and PGV of each station. Gao et al. (2021) also analyzed the influence of the number and distribution of stations on the moment magnitude inversion.

Recently, with the establishment and improvement of GNSS such as GPS, GLONASS, Galileo, and Beidou (BDS), GNSS seismology has been developed from single GPS system to multiple system usage. Research shows that multi-GNSS has significant advantages including improving the special configuration of satellites, shortening convergence time, and reducing observation noise (Geng et al. 2017, 2018; Zhang et al. 2020; Fang et al. 2021).

In this study, we used high-rate observations from 11 GNSS stations of the Crust Movement Observation Network of China (CMONOC) around the Menyuan earthquake region (Qinghai, China) to understand the coseismic dynamic deformation process of the near field (Fig. 1). We compared and analyzed the time series of the station displacement calculated using multi-GNSS observations; obtained the seismic arrival time, epicenter location, and moment magnitude of the Menyuan earthquake; and finally, obtained the coseismic displacement using the continuous observations from 3 days before and after the earthquake. Our study provides authentic data for studying real-time and post-event coseismic displacement, thereby facilitating

a better understanding of the mechanisms of the Menyuan earthquake.

Data and methods

Multi-GNSS data processing

Our study used high-rate (1 Hz) GNSS data from 11 stations, of which six received GPS, GLONASS, and Galileo observations, and the remaining five stations only had GPS and GLONASS observations. The observation period was 17:30:00–18:00:00 on January 7, 2022 (UTC), and encompassed the high-rate dynamic changes at station locations 15 min before and 15 min after the earthquake. We used the PRIDE PPP-AR software package, which was released by the GNSS Research Center, Wuhan University, to process GNSS data in the kinematic precise point positioning (PPP) mode. The PRIDE PPP-AR can process high-rate (up to 50 Hz) data of GPS, GLONASS, Galileo, BDS, and QZSS systems, and resolve integer ambiguity in the case of the bias-SINEX format phase bias (Geng et al. 2019, 2021).

Table 1 shows the multi-GNSS kinematic PPP processing strategies in detail. The ionospheric-free (IF) combinations from GPS L1/L2, GLONASS L1/L2, and Galileo E1/E5a signals were used. Equal weight was

Fig. 1 GNSS stations around the epicenter of the 2022 $M6.9$ Menyuan earthquake. The red triangles represent GNSS stations that can receive GPS, GLONASS, and Galileo signals, and the blue triangles represent GNSS stations that can only receive GPS and GLONASS signals. The red beach ball represents the focal mechanism of the Menyuan earthquake reported by the United States Geological Survey (USGS). The red lines represent the sesimogenic faults, and the black lines represent the fault

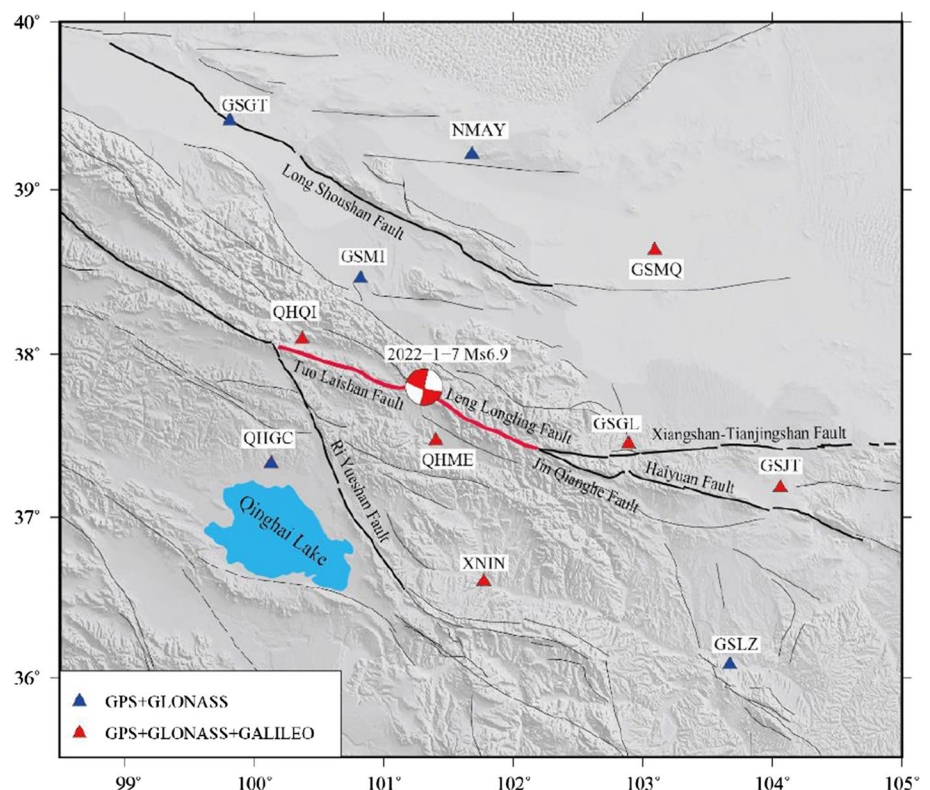


Table 1 Multi-GNSS kinematic PPP processing strategies

Items	Strategies
PPP mode	Ionospheric-free (IF) combination PPP
Observation	GPS/GLONASS/Galileo pseudo range and phase observation
Observation sampling rate	1 Hz
Signal frequency	GPS(L1/L2); GLONASS(L1/L2); Galileo(E1/E5a)
Satellite orbit, clock, and ERP	WUM Rapid product
Cutoff elevation	7°
Estimation method	Least-squares principle of the parameter elimination–recovery method
Coordinate reference system	IGS14
Antenna phase center correction	Corrected using IGS14.atx in ANTEX format
Tropospheric delay	Corrected by Saastamoinen model; estimated (residual wet component)
Ionospheric delay	Eliminated by IF combination
Tide correction	IERS 2010 convention
Cycle slip detection	GF + MW
Ambiguity resolution	LAMBDA for narrow lane and rounding for wide lane

assigned to observations for different satellite systems. Rapid ephemeris, clock error, earth rotation parameters (ERP), and phase clock error/bias products released by Wuhan University’s IGS Analysis Center (denoted as “WUM”) were used in the data processing. The Saastamoinen model (Saastamoinen 1973), combined with the global mapping function (GMF; Boehm et al. 2006) projection, was used to correct tropospheric delay. Residual tropospheric delay was estimated using the random walk process, and the geometry-free (GF) phase combination and Melbourne–Wübbena (MW; Melbourne 1985; Wübbena 1985) combinations to detect cycle slip and eliminate gross errors. The tidal displacements were corrected using the IERS 2010 conventions (Petit and Luzum 2010). The antenna phase center offset (PCO) and phase center variation (PCV) were corrected using an absolute phase center model called IGS14.atx in the antenna exchange format ANTEX (Rothacher and Schmid 2010). Finally, the least-squares method was used to estimate the parameters. The wide lane ambiguity was fixed by rounding method and the narrow lane ambiguity was fixed by the Least-squares AMBIGUITY Decorrelation Adjustment (LAMBDA; Teunissen 1995) method.

Determining the initial arrival time of seismic waves

Accurately extracting the initial arrival time of seismic waves is key to determining earthquake origin time and epicenter location. In this study, the short time average/long time average (STA/LTA) method was used to obtain the initial value of the initial arrival time of seismic waves at each station. When a seismic wave signal arrives, the STA changes faster than the LTA, and the STA/LTA ratio, therefore, increases significantly. When the ratio exceeds a certain

threshold, this epoch can be judged as the arrival time of seismic waves. The STA/LTA formula is expressed as shown below (Allen 1978):

$$\frac{STA_i}{LTA_i} = \frac{\sum_{j=i+1-S}^i CF_j/S}{\sum_{k=i+1-L}^i CF_k/L}, \quad (1)$$

where STA_i and LTA_i represent the average values of eigenfunctions for short time window and long time window, respectively. CF is the eigenfunction, S and L represent the length of short time window and long time window, respectively. We chose 7 s for short time window and 50 s for long time window. The eigenfunction is expressed as shown below (Allen 1982):

$$\begin{cases} CF(i) = x(i)^2 + M[x(i) - x(i-1)]^2 \\ M(i) = \frac{\text{sum}|x(i)|}{\text{sum}|x(i) - x(i-1)|} \end{cases}, \quad (2)$$

where $x(i)$ represents the numerical value of each time series at each epoch.

The STA/LTA method provides only an approximation of the arrival time of seismic waves. Ten sampling points were taken before and after the arrival time, and the Akaike information criterion (AIC) was used to accurately determine the arrival time of seismic waves within this time window. Maeda (1985) proposed a method that can be used to calculate AIC values from seismic recording data:

$$AIC(k) = k \cdot \log \{ \text{var}(x[1, k]) \} + (L - k - 1) \cdot \log \{ \text{var}(x[k + 1, L]) \}, \quad (3)$$

where L is the total number of sampling points in the time window, k is a sampling point, the corresponding range is $[2, L - 2]$, x is the value of time series at one epoch, and var represents the variance over the period. When the AIC

reaches its minimum value, the corresponding epoch is the precise arrival time of the seismic wave.

Inversion of earthquake epicenter and origin time

Theoretically, the three-dimensional (3D) coordinates of a given hypocenter can be inverted using the 3D coordinates of stations and the initial arrival time of seismic waves. However, as GNSS stations surrounding a hypocenter are almost on the same horizontal plane, it is impossible to effectively assess hypocenter depth. Therefore, our study used only GNSS stations coordinates and the initial arrival time of seismic waves to invert the longitude and latitude of the epicenter (Fang et al. 2014b).

If the geodetic coordinates of n GNSS stations are (B_1, L_1) , (B_2, L_2) , ..., (B_n, L_n) , the earthquake arrival times of the n stations are t_1, t_2, \dots, t_n , respectively, and the epicenter position is (B, L) , then the epicenter distance of each station D_i can be expressed as:

$$D_i = \arccos(\sin B_i \times \sin B + \cos B_i \times \cos B \times \cos(L_i - L)) \times R, \quad (4)$$

where B_i is the latitude of station i , L_i is the longitude of station i , and R is the average radius of the earth (6371 km).

Assuming that the propagation velocities of seismic waves in all directions are equal and represented by v , the following equation can be obtained according to the time difference of seismic waves arriving at each observation station:

$$\begin{cases} D_2 - D_1 - v(t_2 - t_1) = 0 \\ D_3 - D_1 - v(t_3 - t_1) = 0 \\ \vdots \\ D_n - D_1 - v(t_n - t_1) = 0. \end{cases} \quad (5)$$

We linearized Eq. (5) and iteratively calculated (B, L) and v based on the least squares to obtain the epicenter coordinates (B, L) and the seismic wave velocity v . The origin time of earthquake T_0 was calculated according to the formula:

$$T_0 = \frac{\sum_{i=1}^n \left(t_i - \frac{D_i}{v} \right)}{n}. \quad (6)$$

Moment magnitude estimation

Earthquake magnitude is a basic parameter that characterizes the strength of an earthquake. The commonly used magnitude scales include surface wave magnitude (M_s) and moment magnitude (M_w). The latter is directly related to

the physical processes of hypocenters and is a mechanical quantity that describes the absolute magnitude of an earthquake. The M_w can be inverted using a regression model using the PGD of a coseismic displacement sequence of the stations. The PGD can be calculated by the formula:

$$\text{PGD} = \max \left(\sqrt{E_d^2(t) + N_d^2(t) + U_d^2(t)} \right), \quad (7)$$

where $E_d(t)$, $N_d(t)$, and $U_d(t)$ show the displacement components of the east, north, and up in centimeters, respectively.

The regression model between PGD and seismic moment magnitude is shown below (Melgar et al. 2015):

$$\log(\text{PGD}) = -4.434 + 1.047 \times M_w - 0.138 \times M_w \times \log(R), \quad (8)$$

where R is the epicenter distance of the GNSS station in km. In this study, the epicentral distance of each station was calculated according to Eq. (4), after which the PGD was calculated according to the coseismic displacement time series of each station.

Results

Displacement waveform results and analysis

To evaluate the performance of the multi-GNSS, this study used three constellation combinations for analysis and comparison: (1) the single GPS system, represented by “GPS”; (2) a combination of GPS and GLONASS, represented by “G + R”; and (3) a combination of GPS, GLONASS, and Galileo, represented by “GRE.” Figure 2 shows the seismic dynamic displacement sequences of the six stations that received GPS, GLONASS, and Galileo observations 10 min before and after the Menyuan earthquake. The horizontal axis represents the time in s after origin time, where zero is the earthquake occurrence time, and the vertical axis represents the displacement time series of each station. The epicentral distance of each station was also marked after the station name.

The results of the three data combinations show that the changes of position in the northern and eastern components of each station clearly reflect the waveform changes after the seismic waves arrived. After the seismic waves reached the stations, the horizontal position of each station experienced slight tremors before occurrence of more violent jumps. Then, recovery tremors occurred gradually after the maximum amplitude of displacement until final stabilization. The QHME station, the station closest to the epicenter location, had the largest horizontal displacement, and a coseismic response with a maximum displacement

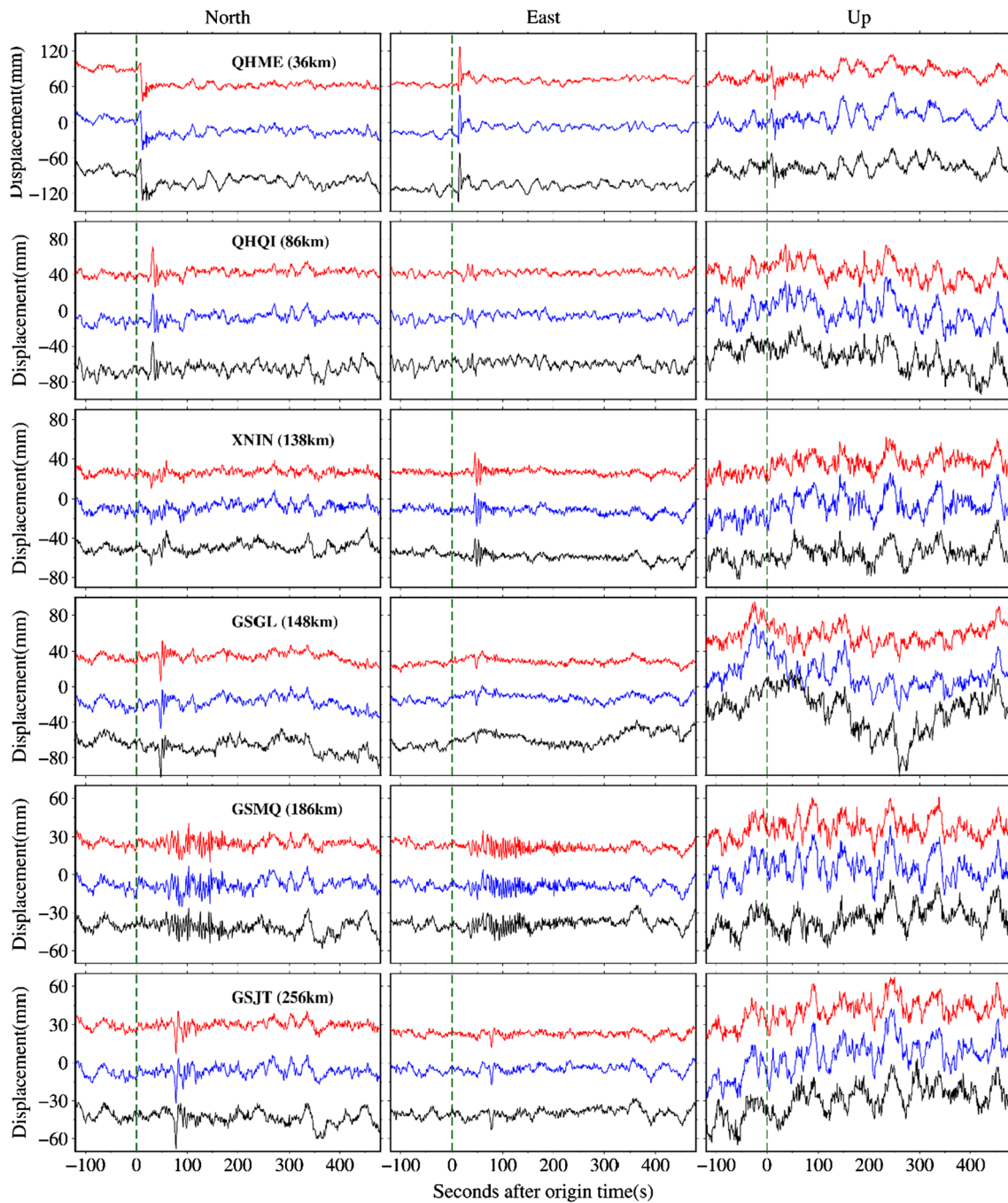


Fig. 2 Displacement time series during the period from 17:43:27 to 17:53:27 (UTC) on January 7, 2022. The red lines represent the GRE results, blue lines represent the G+R results, and black lines repre-

sent the GPS results. The green dotted line represents the origin time of earthquake

of ~60 mm in the north component and ~90 mm in the east component. After the tremors stabilized, the station also experienced a permanent displacement, with a deformation of ~30 mm to the south and ~10 mm to the east. Comparable to QHME, other stations experienced various magnitudes of seismic deformation, but most returned to their original positions after the earthquake with no notable

permanent deformation. In the up component, except for station QHME which was closest to the epicenter location and clearly had subsidence, the stations mainly rose and fell periodically and showed no notable seismic waveforms. This may have been because the earthquake had a strike-slip focal mechanism, which has negligible effects in the vertical component. In addition, the GNSS solution

results have a larger error in the up component than in the north and east components; thus, the small up waveform changes were not displayed.

The results calculated by the single GPS data revealed more fluctuations. The results of the multi-GNSS combination were more stable and were most pronounced at the QHME station (closest to the epicenter location). The farther away from the epicenter location, the less the position of the station was affected by seismic waves, and the more easily the fluctuation of its position was obscured by observation

noise. Figure 3 and Table 2 show the root mean square (RMS) of the calculation results of the three data combinations. To avoid the influence of coseismic and post-seismic relaxation deformations, the RMS results in Fig. 3 and Table 2 are statistical results of the time series for each station position 15 min before the earthquake. Figure 3 shows that the addition of GLONASS data can effectively improve the accuracy of the GNSS high-rate dynamic results. Among the 11 calculated stations, except for a slight increase in the RMS of stations GSGL and NMAY in the east component,

Fig. 3 RMS statistics of displacement time series from three data combinations

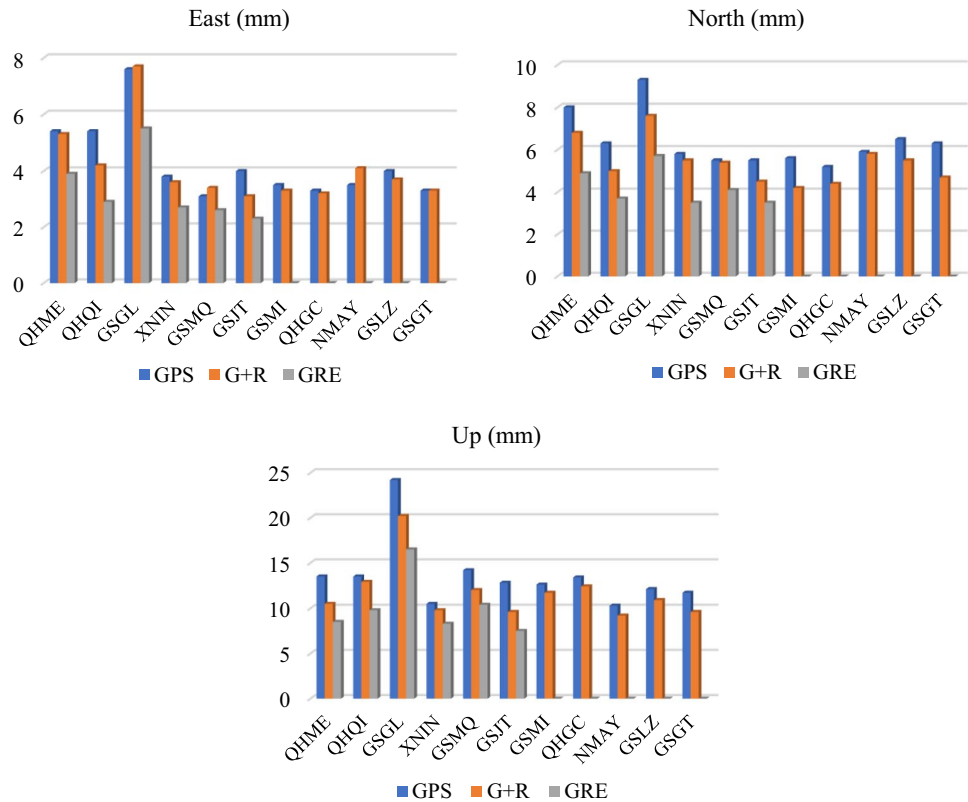


Table 2 RMS of solutions for the high-rate data (mm)

Station code	East			North			Up		
	GPS	G + R	GRE	GPS	G + R	GRE	GPS	G + R	GRE
QHME	5.4	5.3	3.9	8.0	6.8	4.9	13.5	10.5	8.5
QHQI	5.4	4.2	2.9	6.3	5.0	3.7	13.5	12.9	9.8
GSGL	7.6	7.7	5.5	9.3	7.6	5.7	24.2	20.2	16.5
XNIN	3.8	3.6	2.7	5.5	5.4	3.5	10.5	9.8	8.3
GSMQ	3.1	3.4	2.6	5.5	5.4	4.1	14.2	12	10.4
GSJT	4.0	3.1	2.3	5.5	4.5	3.5	12.8	9.6	7.5
GSMI	3.5	3.3	–	5.6	4.2	–	12.6	11.7	–
QHGC	3.3	3.2	–	5.2	4.4	–	13.4	12.4	–
NMAY	3.5	4.1	–	5.9	5.8	–	10.3	9.2	–
GSLZ	4.0	3.7	–	6.5	5.5	–	12.1	10.9	–
GSGT	3.3	3.3	–	6.3	4.7	–	11.7	9.6	–
Average	4.3	4.1	3.3	6.4	5.4	4.2	13.5	11.7	10.2

the RMS of the other stations in three components fell. After adding the Galileo data, the calculation precision of the GRE improved compared with the G+R. The numerical statistical results in Table 2 show that the average RMS values in the north, east, and up components solely using the GPS were 4.3, 6.4, and 13.5 mm. After adding the GLONASS data, they were reduced to 4.1, 5.4, and 11.7 mm, with 4.7, 15.6, and 13.3% better precision, respectively. After adding the Galileo data, the average RMS values became 3.3, 4.2, and 10.2 mm, which represent increases in precision of 23.3, 34.4, and 24.4%, respectively.

Arrival time of seismic wave results

The dynamic displacement time series of stations, calculated using high-rate GNSS data, contains some systematic errors such as multi-path effects, unmodeled antenna phase center variation, and tracking errors, which directly affect the accuracy of the initial arrival time of the seismic waves. To reduce the influence of these noises, this study first differentiated between epochs of the dynamic displacement time series of GNSS stations to obtain the high-rate velocity time series in the north, east, and up components, respectively, as shown in Fig. 4. In the horizontal component, the high-rate

velocity time series of nine stations clearly reflected the propagation characteristics of seismic waves after they arrived at the stations except stations QHGC and GSGT. Concurrently, in the vertical displacement, only QHME, the closest to the epicenter locations of the 11 stations, showed clear seismic deformation. As a result, this study used only the velocity results of stations in the horizontal component to determine the initial arrival time of seismic waves.

Based on the horizontal velocity time series of 11 stations of the three data combinations, combined with the STA/LTA method and AIC criterion, the arrival time of seismic waves was extracted for each station. The extracted results of stations QHGC and GSGT were more than 200 s after the origin time. Considering their distance from the epicenter location, the results were assumed to be incorrect and were discarded. The initial arrival times of seismic waves at the nine other stations are shown in Table 3.

Epicenter and earthquake origin time results

Based on the initial arrival time of seismic waves and the latitude and longitude of each station in Table 3, the epicenter and occurrence time of the Menyuan earthquake were obtained according to Eqs. (4), (5), and (6), as shown

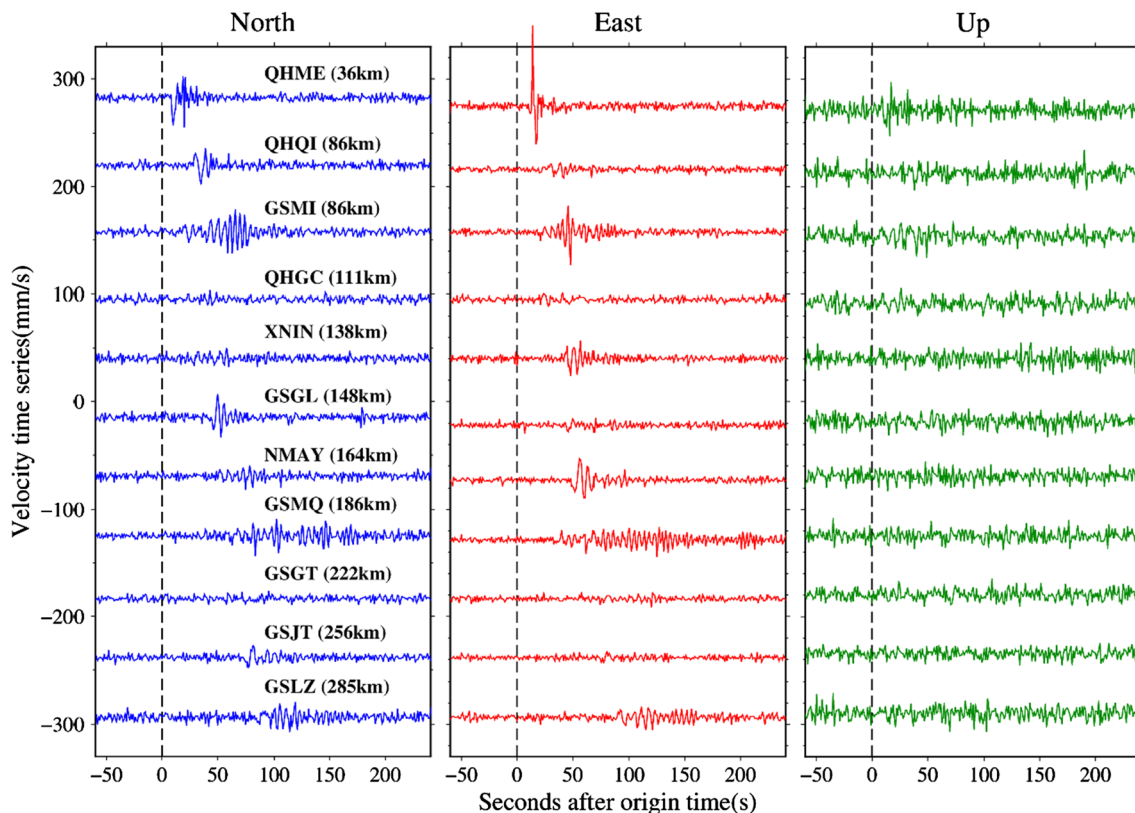


Fig. 4 Velocity time series from 1 Hz GRE data. The blue lines represent the results in north component, red lines represent the results in east component, and green lines represent the vertical results. The black dotted line represents the origin time of earthquake

Table 3 Arrival time of seismic wave at nine stations

Station code	Longitude (°)	Latitude (°)	Arrival time of seismic wave (UTC)		
			GPS	G+R	GRE
QHME	101.40	37.47	17:45:35	17:45:35	17:45:35
QHQI	100.37	38.09	17:45:53	17:45:53	17:45:52
GSMI	100.82	38.46	17:45:52	17:45:52	17:45:52
XNIN	101.77	36.60	17:46:11	17:46:11	17:46:09
GSGL	102.89	37.45	17:46:11	17:46:11	17:46:12
NMAY	101.68	39.21	17:46:18	17:46:15	17:46:15
GSMQ	103.09	38.63	17:46:27	17:46:27	17:46:27
GSJT	104.06	37.18	17:46:41	17:46:41	17:46:40
GSLZ	103.67	36.08	17:46:56	17:46:56	17:46:56

in Table 4. Using the epicenter and earthquake origin time released by China Earthquake Networks Center (CENC) as a reference (Table 4), the distance between the reference epicenter and the epicenter calculated by GRE observations was ~2.8 km, and the difference in the earthquake occurrence time was ~1.9 s. The distance between the reference epicenter and the epicenter calculated by G+R observations was ~3.6 km, and the difference in the earthquake occurrence time was ~2.3 s. The distance between the reference epicenter and the epicenter calculated by

GPS observations was ~3.7 km, and the difference in the earthquake occurrence time was ~2.2 s.

The STA/LTA method used in this study reflects the sudden change in signal or energy through the ratio of the average value of signals within distinct time window lengths. AIC also requires calculation of the minimum variance for a time series. The extracted results of the initial arrival times for the two methods were closely related to the signal-to-noise ratio of the time series. According to the analysis in section “Displacement waveform results and analysis”, the stability and noise level of the time series calculated based on GRE were noticeably better than the results obtained by G+R and GPS. Therefore, the initial arrival time of seismic waves extracted based on the GRE time series was more accurate than that based on the G+R and GPS data. The inversion results for the epicenter location and the occurrence time of the earthquake were also closer to the corresponding reference values.

PGD Results and moment magnitude

The moment magnitude results based on the PGD of all the GNSS stations were estimated by formula (8), as shown in Table 5. Owing to the different crustal structures, bedrock properties, and altitudes at which the stations were located, there are certain discrepancies between the moment

Table 4 Comparison of the Menyuan earthquake source parameters from CENC, USGS, GFZ, and this study

Institution	Epicenter position		Origin time (UTC)	Earthquake magnitude
	Longitude	Latitude		
CENC	101.26	37.77	17:45:27	Ms6.9
USGS	101.290	37.828	17:45:30	Mw6.6
GFZ	101.34	37.81	17:45:32.1	Mw6.6
ThisPaperGPS	101.301	37.764	17:45:24.8	Mw6.64
ThisPaperG+R	101.297	37.783	17:45:24.7	Mw6.66
ThisPaperGRE	101.230	37.761	17:45:25.1	Mw6.62

Table 5 Estimation of moment magnitude of Menyuan earthquake with three data combinations

Station code	Epicenter distance (km)	GPS		G+R		GRE	
		PGD/mm	M_w	PGD/mm	M_w	PGD/mm	M_w
QHME	36	70.4	6.34	71.4	6.35	74.9	6.37
QHQI	86	44.6	6.52	39.9	6.45	32.5	6.34
GSMI	86	34.8	6.38	29.0	6.28	29.0	6.28
QHGC	111	23.6	6.29	29.1	6.40	29.1	6.40
XNIN	138	26.7	6.47	35.9	6.64	26.6	6.46
GSGL	148	61.3	6.98	43.4	6.78	31.8	6.60
NMAY	164	35.2	6.72	40.8	6.81	40.8	6.81
GSMQ	186	22.2	6.52	33.7	6.76	30.3	6.70
GSGT	222	45.5	7.04	26.5	6.72	26.5	6.72
GSJT	256	30.6	6.88	37.2	7.00	44.5	7.11
GSLZ	285	28.9	6.91	35.8	7.04	35.8	7.04

magnitude at different stations estimated by PGD and the actual magnitude. Therefore, more accurate magnitude estimates are usually obtained by averaging the results of as many stations as possible (Fang et al. 2014a; Gao et al. 2021). The average values of all the moment magnitudes estimated by each data combination were 6.64, 6.66, and 6.62, respectively. The M_w values for the Menyuan earthquake released by USGS and GeoForschungsZentrum Potsdam, Germany (GFZ) were both 6.6. Therefore, the estimated result of the GRE is in the best agreement with the results released by the two institutions, with a difference of only 0.02 magnitude units, while the results of the other two combinations are slightly higher. Results of this study verify the effectiveness of high-rate GNSS at quickly estimating M_w .

Discussion

Our results indicate that high-rate multi-GNSS data can provide relatively accurate earthquake source parameter estimation. This is because the stability and noise level of the time series calculated by the GRE combination were significantly better than the results obtained by G + R and GPS. Figure 5 shows the average number of visible satellites and the position dilution of precision (PDOP) for each station. As shown in Fig. 5, with the addition of GLONASS, at least five visible satellites were added for most stations, while the Galileo system was more stable, with at least six satellites visible at each station. The addition of GLONASS and Galileo data more than doubled the number of visible satellites obtained using GPS data, thereby significantly improving the spatial geometry of satellites, substantially reducing PDOP, improving calculation accuracy, and stabilizing the time series and noise remarkably better than the GPS results.

To further evaluate the performance of the multi-GNSS applied for seismogeodesy, the high-rate (1 Hz) GNSS data mentioned above and 30-s sampling interval GNSS data (30 s) were used to calculate the coseismic displacement, respectively. First, to calculate the coseismic deformation of each station with 1 Hz data, it is necessary to eliminate violent fluctuations (Fig. 2); thus, only the relatively smooth parts of displacement time series at each station before and after the earthquake are retained. The averages of displacement time series after the earthquake minus the averages of displacement time series before the earthquake is the coseismic displacement (Li et al. 2021b).

Conventional the GNSS data analysis for crustal deformation monitoring is usually achieved though double-difference (DD) approach to obtain the ambiguity-fixed solutions of station coordinates (Wang and Shen 2020). Geng and Mao (2021) processed one year of GNSS data from 192 globally distributed stations and found that the position repeatability and the RMS error of undifferenced integer ambiguity resolution (UD-IAR) were both better than those of DD integer ambiguity resolution; thus, the UD-IAR for GNSS network analysis was recommended to achieve ambiguity-fixed solutions efficiently. We then processed the 30-s sampling rate multi-GNSS observations with a duration of six days from three days before the earthquake to three days after to obtain the daily solution of coordinates of each station in static PPP mode using PRIDE PPP-AR software. The processing strategies of static PPP were similar to those shown in Table 1. It should be noted that the precise satellite orbit, satellite clock, ERP, phase bias, and satellite attitude quaternions for multi-GNSS experiment (MGEX) released by Center for Orbit Determination in Europe (CODE) were used in static PPP and the wide lane ambiguity and the narrow lane ambiguity were fixed by the same rounding method.

The north, east, and up components of the daily solutions for the 3 days before and after the earthquake were averaged,

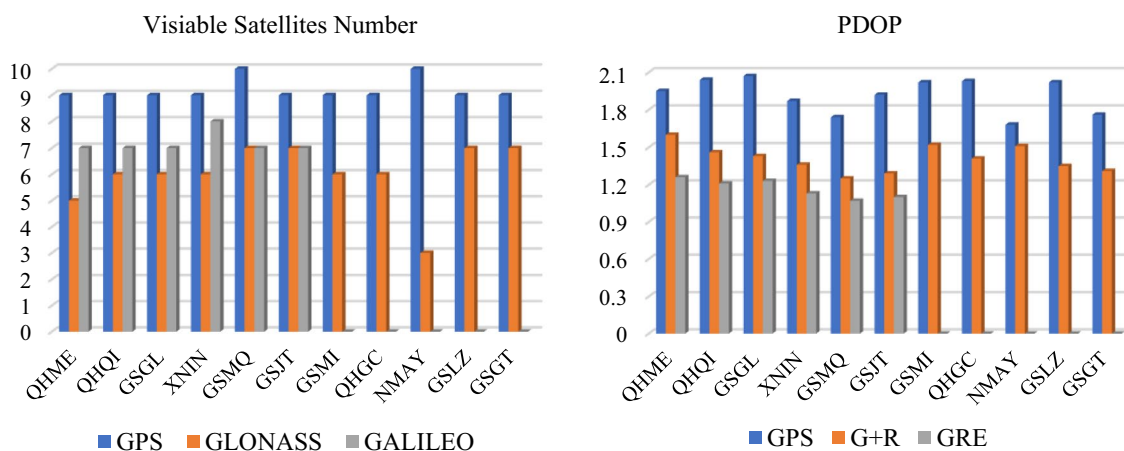


Fig. 5 Average number of visible satellites and the PDOP for each station

Table 6 Coseismic horizontal displacement solved by three data combinations

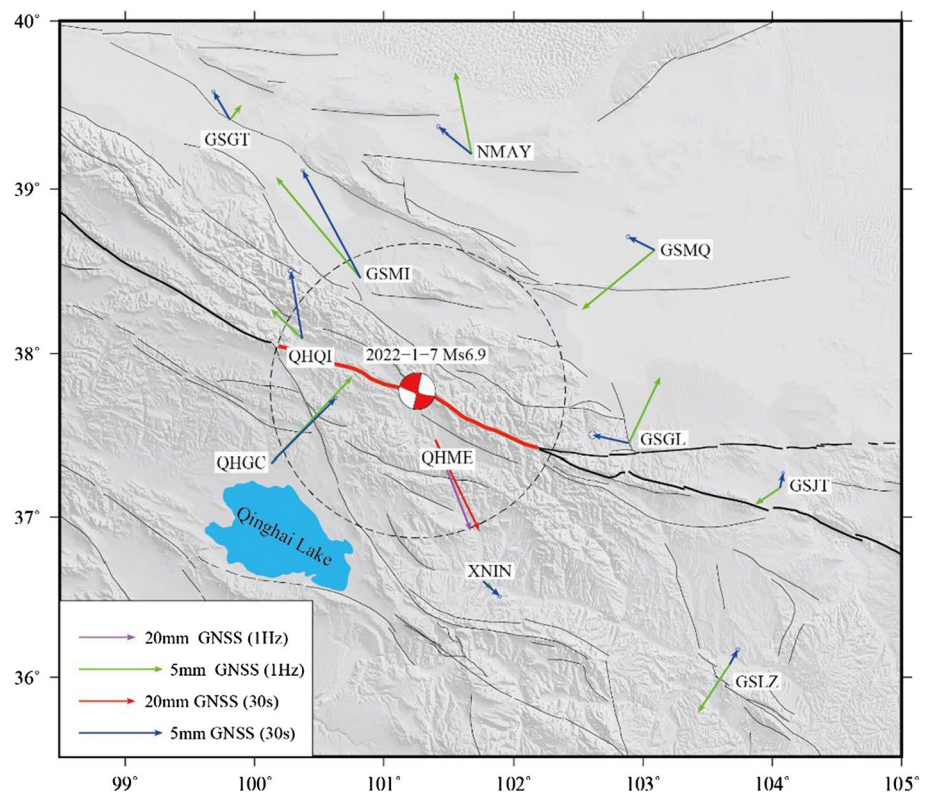
Station code	GPS		G + R		GRE	
	East (mm)	North (mm)	East (mm)	North (mm)	East (mm)	North (mm)
QHME	15.6	−32.5	15.9	−32.5	15.8	−32.6
QHQI	−1.2	3.9	−0.7	4.1	−0.7	4.2
GSGL	−0.5	0.3	−2.2	0.5	−2.2	0.5
XNIN	0.8	−0.8	1.0	−0.9	1.0	−0.9
GSMQ	−2.1	0.6	−1.6	0.8	−1.6	0.8
GSJT	0.1	1	0.2	0.9	0.3	0.7
GSMI	−3.7	6.6	−3.5	6.5	−	−
QHGC	3.7	3.5	3.9	3.9	−	−
NMAY	−1.9	1.6	−2.0	1.6	−	−
GSLZ	−0.1	0.8	0.5	0.9	−	−
GSGT	−1.6	1.7	−1.0	1.7	−	−

after which the pre-earthquake average was subtracted from post-earthquake average to obtain high-precision coseismic deformation (Jiang et al. 2022). Table 6 shows the results of coseismic horizontal displacement based on three data combinations. The results of the different data combinations were highly similar, with a maximum difference of ~1.7 mm. The difference in most of the other results was within 0.5 mm. Considering that the accuracy of the single-day static fixed solution of PRIDE PPP-AR in the horizontal component was 1–2 mm (Geng et al. 2019; Geng and Mao

2021), it can be adjudged that the accuracy of the three data combinations of results is consistent.

Figure 6 shows the coseismic displacement obtained, respectively, from 1 Hz GRE data and multi-day 30 s GRE data. For the four stations within ~100 km of the epicenter location, the coseismic displacement results calculated by the 1 Hz data and the 30 s data were relatively similar, whereas there were greater discrepancies for stations farther away. In terms of the high-rate data results, the magnitudes of coseismic deformation of stations far from the epicenter location were extremely small and easily obscured by the

Fig. 6 Coseismic displacement obtained, respectively, from high-rate GRE data (1 Hz) and multi-day GRE solutions (30 s). The purple and green arrows represent the coseismic displacements based on 1 Hz data, and the red and blue arrows represent the coseismic displacements based on the 30 s data. The black dotted circle indicates the range within 100 km of the epicenter



noise in the observations. In the high-rate dynamic displacement time series of each station, the coordinates of each epoch were only estimated by the GNSS observations at that epoch, while for the daily solution of 30 s data, the coordinates of the station were estimated by the GNSS observations of 24 h. Most of errors were eliminated or attenuated by averaging; thus, errors were small, providing a more accurate reflection of actual coseismic deformation.

The coseismic displacement results show that the stations located on the north side of the seismogenic fault experienced clear northwest movement. Only stations QHME and QHGC on the south side of the seismogenic fault are relatively close and reflect clear coseismic displacement. Stations XNIN and GSLZ are relatively far away, of which calculated results of coseismic displacement are all within 1 mm, which is less than the error. Station QHME, closest to the epicenter location, suffered substantial permanent deformation, with an eastward displacement of ~15.8 mm and a southward displacement of ~32.6 mm. The coseismic displacement results in this study reflect the left-lateral strike-slip focal mechanism of the Menyuan earthquake and are consistent with the conclusions drawn from field investigations, hypocenter parameters, aftershock distribution, and Interferometric Synthetic Aperture Radar (InSAR) inversion (Li et al. 2022a, 2022b; Pan et al. 2022).

Conclusions

This study used the PPP method to process the high-rate GNSS data of 11 stations near the Menyuan earthquake in Qinghai, China, as well as the continuous observation data from six days before and after the earthquake. The following conclusions were obtained through our analysis:

In the processing of high-rate GNSS data, the multi-GNSS was found to be relatively accurate. Compared with that based on the single GPS, the RMS values of the displacement time series based on GPS/GLONASS/Galileo in the three components of north, east, and up reduced 23.3, 34.4, and 24.4%, respectively. GPS/GLONASS/Galileo combination remarkably increased the number of visible satellites and enhanced the spatial geometry of satellites, thereby improving positioning accuracy and dynamic solution stability. For the coseismic displacement calculated in the static PPP mode, the results of the multi-GNSS and the single GPS system were very close, with no apparent improvement in accuracy.

The estimations of the Menyuan earthquake source parameters show that results from the GPS/GLONASS/Galileo coseismic time series were more accurate than those obtained from other time series. The earthquake origin time with GPS/GLONASS/Galileo was 17:45:25.1, the epicenter was 37.761 N, 101.230 E, and the M_w was 6.62.

Their differences from the origin time and epicenter of CENC were 1.9 s and 2.8 km, respectively. The M_w results were most consistent with the results of UCGS and GFZ, with a difference of only 0.02 magnitude units. Using high-rate multi-GNSS observations can enable the acquisition of more accurate seismic parameters, thereby improving technical and data support in applications such as earthquake warning systems and post-earthquake rescue efforts.

Comparing the coseismic displacement calculated by the 15-min high-rate data dynamic solution and the multi-day static solution, the results at nearby stations were relatively similar in terms of size and direction, while the results at distant stations using high-rate data were less than the observation error due to the higher noise level. Coseismic displacement calculated from multi-day static solutions were found to be relatively accurate and reliable.

Authors' contributions Not applicable.

Funding This work was funded by grants from the National Natural Science Foundation of China (No. 41974011), the Natural Science Foundation of Tianjin city (No. 20JCQNJC01360), and the Earthquake Tracking Track of China Earthquake Administration (CEA; 2022010211).

Availability of data and material Not applicable.

Code availability Not applicable.

Declarations

Conflict of interest On behalf of all authors, the corresponding author states that there is no conflict of interest.

References

- Allen RV (1978) Automatic earthquake recognition and timing from single traces. *Bull Seismol Soc Am* 68(5):1521–1532
- Allen RV (1982) Automatic phase pickers: their present use and future prospects. *Bull Seismol Soc Am* 72(6B):S225–S242
- Boehm J, Niell A, Tregoning P et al (2006) Global mapping function (GMF): a new empirical mapping function based on numerical weather model data. *Geophys Res Lett* 33:L07304
- Fang RX, Lv HH, Shu YM et al (2021) Improved performance of GNSS precise point positioning for high-rate seismogeodesy with recent BDS-3 and Galileo. *Adv Space Res* 68:3255–3267
- Fang RX, Shi C, Song WW et al (2014a) Determination of earthquake magnitude using GPS displacement waveforms from real-time precise point positioning. *Geophys J Int* 196:461–472
- Fang RX, Shi C, Wang GX et al (2014b) Epicenter and magnitude of large earthquake determined from high-rate GPS observations: a case study of the 2008 M8.0 Wenchuan Earthquake. *Sci China Earth Sci*. <https://doi.org/10.1007/s11430-013-4803-2>
- Fang RX, Zheng JW, Geng JH et al (2020) Earthquake magnitude scaling using peak ground velocity derived from High-Rate GNSS observations. *Seismol Res Lett* 92(1):227–237
- Gao ZY, Li YC, Shan XJ et al (2021) Earthquake magnitude estimation from high-rate GNSS data: a case study of the 2021 Mw 7.3 Maduo earthquake. *Remote Sens* 13:4478

- Geng JH, Mao SY (2021) Massive GNSS network analysis without baselines: undifferenced ambiguity resolution. *J Geophys Res Solid Earth* 126:e2020JB021558
- Geng JH, Jiang P, Liu JN et al (2017) Integrating GPS with GLONASS for high-rate seismogeodesy. *Geophys Res Lett* 44:3139–3146
- Geng JH, Pan YX, Li XT et al (2018) Noise characteristics of high-rate multi-GNSS for subdaily crustal deformation monitoring. *J Geophys Res* 123(2):1987–2002
- Geng JH, Chen XY, Pan YX et al (2019) PRIDE PPP-AR: an open-source software for GPS PPP ambiguity resolution. *GPS Solutions* 23:91
- Geng JH, Yang SF, Guo J (2021) Assessing IGS GPS/Galileo/BDS-2/BDS-3 phase bias products with PRIDE PPP-AR. *Satell Navig* 2(1):1–15
- Jiang WP, Xu CJ, Li ZW et al (2022) Using space observation techniques to study temporal and spatial characteristics of seismogenic process, occurrence and deformation of the Qinghai Madoi Mw 7.4 earthquake. *Chin J Geophys* 65(2):495–508. <https://doi.org/10.6038/cjg2022P0732>. (in Chinese)
- Li JW, Chen CY, Zhan W et al (2021a) Research on fast acquisition of GNSS coseismic horizontal displacement of Madoi Ms7.4 earthquake in Qinghai Province. *Seismol Geol* 43(5):1073–1084
- Li ZC, Ding KH, Zhang P et al (2021b) Coseismic deformation and slip distribution of 2021 Mw 7.4 Madoi earthquake from GNSS observations. *Geomat Inf Sci Wuhan Univ* 46(10):1489–1497 (in Chinese)
- Li ZH, Han BQ, Liu ZJ et al (2022a) Source parameters and slip distributions of the 2016 and 2022a Menyuan, Qinghai earthquakes constrained by InSAR observations. *Geomatics and Information Science of Wuhan University* <https://doi.org/10.13203/j.whugis20220037>
- Li ZM, Gai HL, Li X et al (2022b) Seismogenic fault and coseismic surfaces deformation of the Menyuan Ms6.9 earthquake in Qinghai. *Acta Geol Sin* 96(1):330–335 (in Chinese)
- Maeda N (1985) A method for reading and checking phase times in autoprocesing system of seismic wave data. *Zisin Jishin* 38:365–379
- Melbourne WG (1985) The case for ranging in GPS-based geodetic systems. In: *Proceeding of 1st international symposium on precise positioning with the global positioning system*, April 15–19, Rockville, pp 373–386
- Melgar D, Crowell BW, Geng JH et al (2015) Earthquake magnitude calculation without saturation from the scaling of peak ground displacement. *Geophys Res Lett* 42:5197–5205
- Pan JW, Li HB, Marie LC et al (2022) Coseismic surface rupture and seismogenic structure of the 2022 Ms6.9 Menyuan earthquake, Qinghai Province, China. *Acta Geol Sin* 96(1):215–231 (in Chinese)
- Petit G, Luzum B (2010) IERS Conventions 2010, IERS Tech. Note 36. Verlag des Bundesamtes für Kartographie und Geodäsie, Frankfurt am Mian, Germany
- Rothacher M, Schmid R (2010) ANTEX: the antenna exchange format, version 1.4. IGS Central Bureau, Pasadena
- Saastamoinen J (1973) Contributions to the theory of atmospheric refraction. *Bull Géod* 47:13–34
- Shan XJ, Yin H, Liu XD et al (2019) High-rate real-time GNSS seismology and early warning of earthquakes. *Chin J Geophys* 62(8):3043–3052
- Teunissen PJG (1995) The least-squares ambiguity decorrelation adjustment: a method for fast GPS integer ambiguity estimation. *J Geod* 70:65–82
- Wang M, Shen ZK (2020) Present-day crustal deformation of continental China derived from GPS and its tectonic implications. *J Geophys Res Solid Earth* 125:e2019JB018774
- Wübbena G (1985) Software developments for geodetic positioning with GPS using TI-4100 code and carrier measurements. In: *Proceeding of 1st international symposium on precise positioning with the global positioning system*, April 15–19, Rockville, pp 403–412
- Yin HT, Zhang PZ, Gan WJ et al (2010) Near-field surface movement during the Wenchuan Ms8.0 earthquake measured by high-rate GPS. *Chin Sci Bull* 26(55):2621–2626
- Yin H, Shan XJ, Zhang YF et al (2018) Rapid determination of source parameters for the 2008 Wenchuan earthquake constrained by high-rate GPS and strong motion data. *Chin J Geophys* 61(5):1806–1816 (in Chinese)
- Zhang XH, Hu JH, Ren XD (2020) New progress of PPP/PPP-RTK and positioning performance comparison of BDS/GNSS PPP. *Acta Geodaetica Et Cartographica Sinica* 49(9):1084–1100 (in Chinese)

Springer Nature or its licensor (e.g. a society or other partner) holds exclusive rights to this article under a publishing agreement with the author(s) or other rightsholder(s); author self-archiving of the accepted manuscript version of this article is solely governed by the terms of such publishing agreement and applicable law.